Clim Dyn
DOI 10.1007/s00382-017-3598-9

Changes in atmospheric rivers and moisture transport over the Northeast Pacific and western North America in response to ENSO diversity

Hye-Mi Kim[1] · **Yang Zhou**[1] · **Michael A. Alexander**[2]

Received: 1 June 2016 / Accepted: 20 February 2017

Abstract The year-to-year changes in atmospheric rivers (ARs) and moisture transport over the northeast Pacific and western North America are investigated during December to February (DJF) from 1979/80 to 2015/16. Changes in AR frequency, intensity, and landfall characteristics are compared between three ENSO phases: central Pacific El Niño (CPEN), eastern Pacific El Niño (EPEN), and La Niña (NINA). During EPEN events, the subtropical jet extends to the south and east with an anomalous cyclonic flow around a deeper Aleutian Low. More moisture is transported towards North America and AR frequency is increased over western North America. In CPEN events, the Aleutian low shifts further southward relative to its position in EPEN, resulting in an increase in the frequency and intensity of landfalling ARs over the southwestern US. In NINA events, the landfalling AR frequency is reduced associated with anomalous anticyclonic circulation over the eastern North Pacific. We diagnose the contribution of multiple factors to the seasonal mean moisture transport using moisture budgets. During the three ENSO phases, the change in low-frequency circulation (dynamical process) is the leading contributor to the seasonal mean moisture flux divergence, while the contributions of the synoptic anomalies and the change in moisture anomaly (thermodynamic process) are not significant along the west coast of North America.

This paper is a contribution to the special collection on ENSO Diversity. The special collection aims at improving understanding of the origin, evolution, and impacts of ENSO events that differ in amplitude and spatial patterns, in both observational and modeling contexts, and in the current as well as future climate scenarios. This special collection is coordinated by Antonietta Capotondi, Eric Guilyardi, Ben Kirtman and Sang-Wook Yeh.

✉ Hye-Mi Kim
hyemi.kim@stonybrook.edu

[1] School of Marine and Atmospheric Sciences, Stony Brook University, Stony Brook, NY 11794, USA

[2] NOAA/Earth System Research Laboratory, Boulder, CO, USA

1 Introduction

Atmospheric moisture transport plays a significant role in the global hydrological cycle. The poleward atmospheric moisture transport in midlatitudes during winter is predominantly confined to Atmospheric Rivers (ARs, Newell et al. 1992; Zhu and Newell 1998), which are filamentary features. Generally, ARs develop over a short time (<10 days) and form as spatially narrow plumes (500–1000 km wide) of water vapor transport that can stretch over thousands of kilometers in the troposphere. ARs are characterized by high water vapor content and occur ahead of cold fronts associated with winter storms. (e.g., as reviewed in Gimeno et al. 2014). While ARs are mainly found over the oceans, their occurrence varies by location, season, and by changes in the background state associated with low-frequency climate variability. The maximum AR frequency is found in northeastern Pacific but with fairly frequent landfalls along the west coast of North America, especially during winter (e.g., Guan and Waliser 2015). Landfalling ARs often induce heavy wintertime precipitation over the western US caused by the enhanced moisture transport (e.g., Dettinger 2006; Neiman et al. 2008) and strong orographic forcing (e.g. Smith et al. 2010). Severe flood events that occurred in California and Pacific Northwest were coincident with AR events (Ralph et al. 2006; Smith et al. 2010; Dettinger et al. 2011; Neiman et al. 2011). The moisture

Published online: 16 March 2017

from ARs also penetrates into the Intermountain Western US causing extreme precipitation events in states such as Arizona, Idaho and Utah (Rutz et al. 2014, 2015; Alexander et al. 2015).

ARs have been mainly studied on timescales shorter than 2 weeks since they are closely associated with synoptic weather. Only several recent studies have begun to explore the link between the ARs and low-frequency climate variability, such as the El Niño Southern Oscillation (ENSO). Dettinger (2006) and Bao et al. (2006) found that the neutral ENSO phase provides the most favorable conditions for the direct entrainment of tropical moisture into the west coast of North America, while later studies reached a different conclusion. For example, Guan and Waliser (2015) showed that ARs are significantly modulated by the low-frequency variability, such as ENSO, Madden-Julian Oscillation (MJO), Arctic Oscillation (AO) and Pacific-North America (PNA), consistent with their previous studies (Guan et al. 2012, 2013). They concluded that AR events are more frequent in El Niño relative to La Niña winters, particularly along the west coast of North America. Ryoo et al. (2013) also found a stronger moisture transport into the western US during El Niño than La Niña winters induced by enhanced cyclonic wave breaking associated with a stronger subtropical jet in El Niño winters. Payne and Magnusdottir (2014) and Mundhenk et al. (2016) reached a similar conclusion with more frequent ARs in El Niño relative to La Niña winters along the west coast of North America.

The SST anomalies associated with ENSO in the tropical Pacific have exhibited a wide range of patterns and amplitudes, and this diversity influences tropical precipitation which in turn forces the large-scale atmospheric circulation anomalies (e.g., Smith and Sardeshmukh 2000; Yu and Zou 2013; Capotondi et al. 2015). Kim and Alexander (2015) showed that the moisture transport in the northeast Pacific was substantially different during central Pacific (CP) El Niños which have maximum SST near the dateline, versus Eastern Pacific (EP) El Niños which have maximum SST in the East Pacific. During EP El Niño winters, positive moisture transport anomalies extend northeastward from the subtropical Pacific towards the west coast of North America by following the anomalous cyclonic flow associated with a deeper Aleutian low. In CP El Niño winters, the subtropical jet and Aleutian low are located further south, which induce more moisture transport into the southwestern US. Associated with the moisture transport in different ENSO phases, the precipitation anomalies differ over the western US. While the moisture transport in the northeast Pacific has been investigated by Kim and Alexander (2015), direct comparison of AR activity and its characteristics in different ENSO phases, have not been examined. Here we will examine the extent to which AR frequency, intensity, and landfall location change between EP and CP El Niño and La Niña events as well.

During El Niño the horizontal extension of the subtropical jet results in more zonal moisture transport towards the west coast of the US, while in La Niña winters, the jet splits into northern and southern branches near the jet exit region (e.g., Ryoo et al. 2013). In addition, most of the precipitation during winter over the western US comes from the passage of extratropical cyclones. For example, winter precipitation in California increases significantly with enhanced extratropical cyclone activity (Chang et al. 2015). Therefore, while moisture transport over the Pacific is modulated by low-frequency variability, it is ultimately tied to synoptic phenomena especially extratropical cyclones. Although the moisture is largely transported by the mean flow, synoptic and low-frequency anomalies also transport a significant amount of moisture, especially near the west coast of North America (Newman et al. 2012; Ryoo et al. 2013). In this study, we will apply moisture budget analyses to quantify the moisture transport by low-frequency and synoptic anomalies during EP El Niño (EPEN), CP El Niño (CPEN) and La Niña (NINA) events.

The change of moisture transport could arise from either change in moisture (thermodynamic process), changes in the circulation (dynamic process), or non-linear terms involving changes in both. By comparing simulations of the twentieth century and projections of the twenty-first century with the A1B emission scenario, Seager et al. (2012) found that the interannual variability of moisture flux divergence associated with ENSO is mainly driven by changes in circulation, while radiatively forced P–E change is due to the increase in specific humidity as well as change in circulation. In this study, we will quantify the relative contribution of the dynamic and thermodynamic processes to the change of moisture flux divergence, during EPEN, CPEN, and NINA events.

The data and methodology are described in Sect. 2. In Sect. 3, we examine the characteristics of ARs (frequency, intensity and landfall location) during CPEN, EPEN, and NINA, the three ENSO phases defined here. The relative contribution of different processes to the seasonal mean moisture transport in the three ENSO phase are compared in Sect. 4. The results are summarized and discussed in Sect. 5.

2 Data and methodology

Six-hourly and monthly mean data from the European Centre for Medium-Range Weather Forecasts Interim Reanalysis (ERAI, Dee et al. 2011) are used in this study. Horizontal winds and specific humidity (1000–300 hPa, a total of 20 levels) are selected to calculate the vertically integrated

moisture flux. The Hadley Centre Global Sea Ice and Sea Surface Temperature (HadISST, Rayner et al. 2003) is used to define the ENSO years. Both the ERAI and HadISST datasets are retrieved on 1° lat × 1° lon grid. Monthly precipitation data is from the Climate Prediction Center merged analysis of precipitation (CMAP) at 2.5° × 2.5° spatial resolution (Xie and Arkin 1997). The results are presented for December to February (DJF) from 1979/80 to 2015/16, a total 37 years. We have divided the ENSO phases into three categories based on the selection criteria of Kim et al. (2009): EPEN if Niño 3 index is greater than one standard deviation (σ), CPEN if Niño 4 exceeds 0.75σ with Nino 3 below 1.0σ, and NINA if Niño 3.4 is less than −1.0σ. Four EPEN (1982/83, 1991/92, 1997/98, 2015/16), four CPEN (1994/95, 2002/03, 2004/05, 2009/10) and six NINA (1984/85, 1988/89, 1998/99, 1999/2000, 2007/08, 2010/11) events were selected based on these criteria. Bootstrap technique and Student's *t* test are used to determine the statistical significance of the results. In a bootstrap method, a composite anomaly for EPEN, for example, is constructed with 4 years chosen at random from among the 37 years. Then this process is repeated 10,000 times to obtain a probability distribution function.

2.1 AR detection

To detect ARs, first we compute the vertically integrated moisture flux Q in pressure coordinate defined as:

$$Q = \frac{100}{g}\int_{1000}^{300} Vqdp = \langle Vq \rangle \tag{1}$$

where g is the acceleration due to gravity (m s^{-2}), q is specific humidity (kg kg^{-1}), p is pressure (hPa), V is horizontal wind vector (m s^{-1}). Angle brackets indicate the mass-weighted vertical integral from the surface (1000 hPa) to 300 hPa. The daily mean moisture flux is calculated from 6-hourly moisture flux. Our results are not sensitive to the choice of 6-hourly or daily data. We choose vertically integrated moisture flux rather than the integrated moisture due to its strong relationship with the precipitation over the western US. Similar to Rutz et al. (2014), we define an AR event when the daily moisture flux ≥250 kg m^{-1} s^{-1} for a contiguous area ≥2000 km in length. First, for each day, we select events by finding the grid cells where the moisture flux exceeds the threshold value of 250 kg m^{-1} s^{-1}, which corresponds well with the 85th percentile of moisture flux in the northeast Pacific (Guan and Waliser 2015). Then the maximum distance between the boundary grid cells of the selected features are calculated. Features that are longer than 2000 km are defined as an AR event. Although the width and direction of the features are not considered, the selected events possess AR characteristics (Rutz et al. 2014). Note that the AR frequency is the number of days when an AR is detected over a given grid point rather than a number of individual AR events. Hereafter, we simply refer to it as AR frequency. AR frequency in each winter is calculated as the total number of AR days and the AR frequency anomaly is calculated by subtracting the climatology. Details of the detection method for identifying landfalling ARs is described in Sect. 3.

2.2 Eulerian moisture budget analysis

To examine the relative contribution of low-frequency and synoptic anomalies to the total moisture flux, we utilize the moisture budget equation. From the equation of state, hydrostatic equation and continuity equation, the Eulerian moisture budget can be written as:

$$\frac{\partial \langle q \rangle}{\partial t} + \nabla \cdot Q = E - P \tag{2}$$

where P is the precipitation rate and E is the evaporation rate from the surface. Brackets indicate the mass-weighted vertical integral. The equation indicates that $E - P$ is balanced by the convergence of the moisture flux (Q) and by the local rate of change of water vapor storage in the column (e.g., Trenberth 1991; Peixoto and Oort 1992). The first left-hand-side term $\left(\frac{\partial \langle q \rangle}{\partial t}\right)$ is small enough to be neglected in the seasonal mean. By applying Reynolds decomposition and temporal average, the term moisture flux $\left(\bar{Q}\right)$ can be written into a form of mean and eddy components such as:

$$\bar{Q} = \bar{Q}^m + \bar{Q}^{LF} + \bar{Q}^s + \bar{Q}^R \tag{3}$$

where the overbar is the long-term mean, the superscripts are seasonal mean (m) and anomalies for low frequency (LF), synoptic (s), and residual (R) terms. It indicates that total mean moisture transport $\bar{Q}$ can be decomposed into mean moisture transport by the seasonal mean flow $\left(\bar{Q}^m\right)$, low-frequency anomalies $\left(\bar{Q}^{LF}\right)$, synoptic anomalies $\left(\bar{Q}^s\right)$, and the rest of the other terms $\left(\bar{Q}^R\right)$ which is negligible (not shown) (e.g., Newman et al. 2012). A Lanczos filter is applied retaining periods greater than 10 days for low-frequency anomalies and less than 10 days for synoptic anomalies.

3 Atmospheric rivers in the three ENSO phases

3.1 ENSO and AR frequency

The composites of anomalous SST, sea-level pressure (SLP), geopotential height at 500 hPa (Z500) and zonal wind at 300 hPa (U300) for the three ENSO phases during

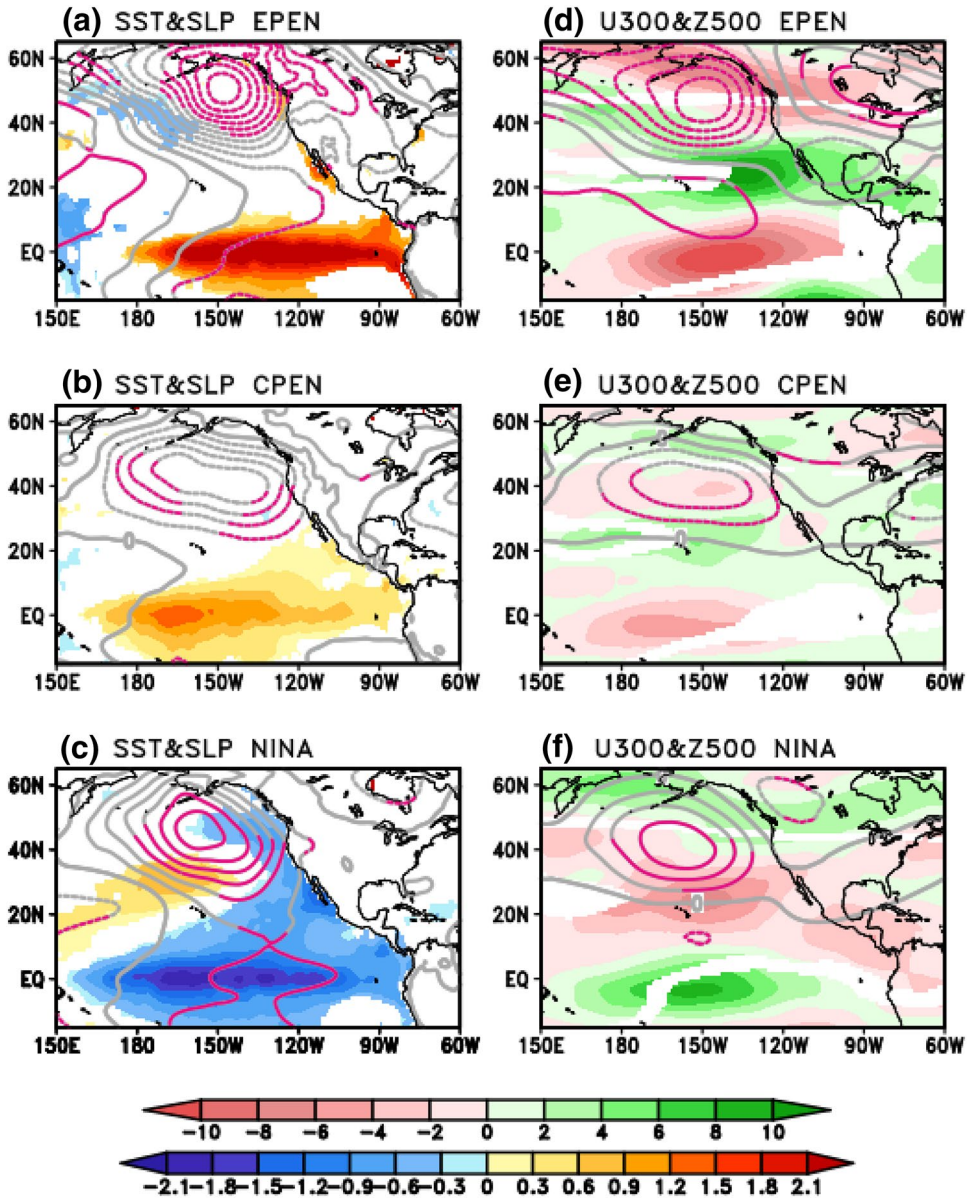

Fig. 1 Composite maps of anomalous **a**–**c** SST (*shadings*, K) and SLP (100 Pa contour interval) and **d**–**f** U300 (*shading*, m s^{-1}) and Z500 (20 m contour interval) for (*top*) EPEN, (*middle*) CPEN, and (*bottom*) NINA. *Shadings* and *magenta lines* have exceeded the 95% significant level based on **a**–**c** Student's *t* test and **d**–**f** bootstrap method

DJF are shown in Fig. 1. The locations of the jet streams during winter can be identified by U300. During EPEN, the anomalous warm SST is confined to the tropical east Pacific associated with a deepened Aleutian Low (Fig. 1a). The subtropical jet shifts equatorward during EPEN inducing strong westerlies in the south (Fig. 1d). During CPEN, the anomalously warm water is located near the dateline in the equatorial Pacific with a deepened Aleutian Low (Fig. 1a). The subtropical jet and the center of the low anomaly are weaker, and the anomalous cyclonic flow shifted southward compared to EPEN (Fig. 1e). During NINA, the SST and circulation patterns are almost opposite to the El Niño winters (both EPEN and CPEN) (Fig. 1c, f). The subtropical jet during NINA is shifted to the north and weaker than in the climatology over the eastern Pacific. The anomalous SSTs and the associated large-scale atmospheric circulation patterns in the three ENSO phases are consistent with previous studies (Capotondi et al. 2015 and references therein).

Due to the shift of the subtropical jet and Aleutian low, the moisture flux is significantly changed over the west coast of North America in the three ENSO phases (Kim and Alexander 2015). Therefore, one can expect changes in characteristics of ARs as well. Figure 2 shows the climatology of moisture flux (vector) and AR frequency (shading) and their anomalies in three ENSO phases in the northeast Pacific and over the western US. Climatologically, the area of high AR frequency (>10 days/winter) is over the northeast Pacific Ocean and west coast of North America (Fig. 2d). During EPEN, the subtropical jet extends to the east with the anomalous cyclonic flow around a deeper

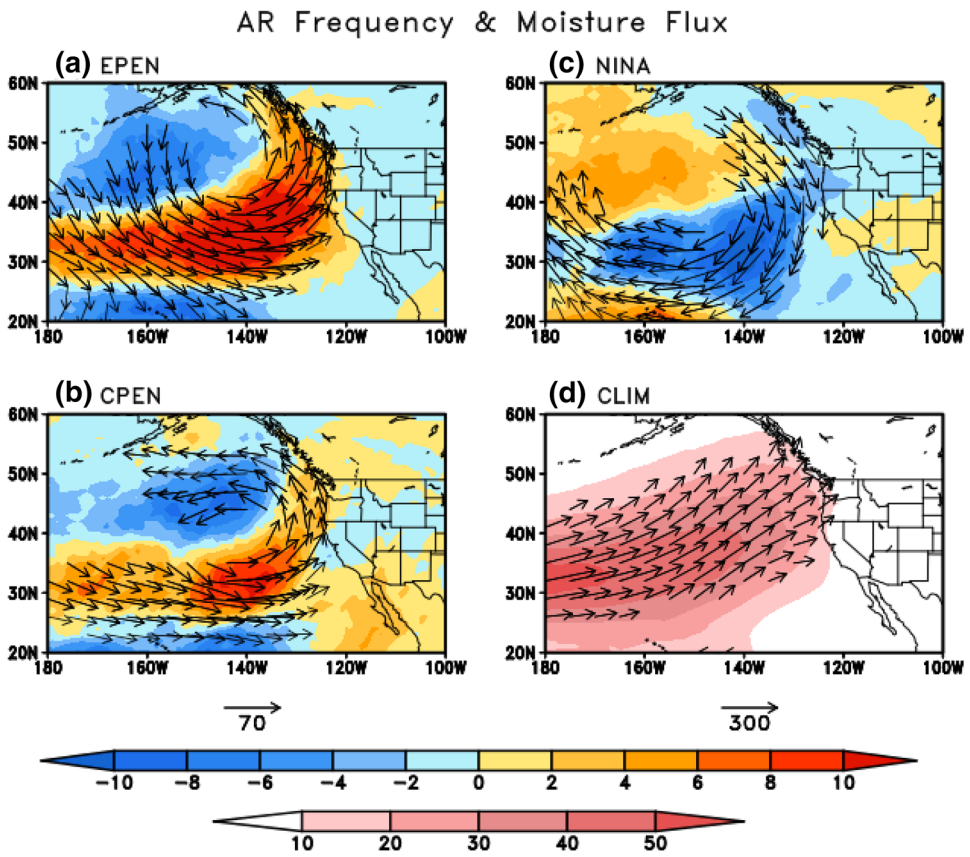

Fig. 2 AR frequency (*shading*, days per winter) and moisture flux (vectors, kg m^{-1} s^{-1}) for **d** climatology and anomalies for **a** EPEN, **b** CPEN, and **c** NINA. The vectors have exceeded the 95% significance level based on a bootstrap method

Aleutian Low (Fig. 1a). Due to the cyclonic anomalies, more moisture from the midlatitudes is transported towards North America (Fig. 2a). The atmospheric response to CPEN includes a southward shift in the Aleutian Low with a zonal extension into the southwest US (Fig. 1b) transporting more moisture into the southwest US (Fig. 2b). During NINA (Fig. 2c), the circulation and AR frequency anomalies are almost opposite to both EPEN and CPEN, with anomalous anticyclonic circulation in the eastern North Pacific (Fig. 2c).

3.2 Characteristics of landfalling ARs

Different circulation patterns associated with the three ENSO phases could result in different AR landfall characteristics, such as landfall frequency, location, and intensity. Figure 3 shows an example of a strong landfalling AR that occurred on 28 January 2016. A region along the west coast of North America is used to determine the intensity and location of landfalling ARs. Similar to the method of Payne and Magnusdottir (2014), at each latitude point, seven grid points in longitude centered on the coastline from 20°N to 60°N (total 287 grid points) are used to detect landfalling ARs. For each day, the zonal average of daily moisture flux is calculated at each latitude in the coastal area. Then, the landfall location is defined by the latitude of the maximum zonal-averaged moisture flux (Q) for each day. The landfall intensity is defined by the maximum value of the zonal-averaged moisture flux (Q). For example, for the landfalling AR case in 28 January 2016 (Fig. 3a), the peak landfall latitude is recorded as 46°N and the intensity as 538.8 kg m^{-1} s^{-1} (Fig. 3b). Only an event with peak landfall intensity larger than 250 kg m^{-1} s^{-1} is defined as a landfalling AR and an event that exceeds 450 kg m^{-1} s^{-1} is defined as an extreme landfalling AR.

During the 37-year record, about 37 landfalling ARs days occurred per winter with a mean location between northern California and Oregon (43.1°N) and mean landfall intensity of 393.8 kg m^{-1} s^{-1} (Table 1). The average number of landfalling ARs is significantly higher than climatology in CPEN (39.8/year) and the highest in EPEN (40.5/year), while it is not significant but lower during NINA (35.2/year) (Table 1). There is no statistically significant difference in landfalling AR frequency between EPEN and CPEN. The frequency of landfalling ARs increases significantly for Baja California and California (20°N–40°N) during CPEN (Table 1), consistent with Figs. 1 and 2. The mean landfall intensity is the strongest in CPEN (408.1 kg m^{-1} s^{-1}), close to normal in EPEN and significantly weaker than normal in NINA (Table 1). The mean landfall intensity is significantly different (at 95% significance level) between

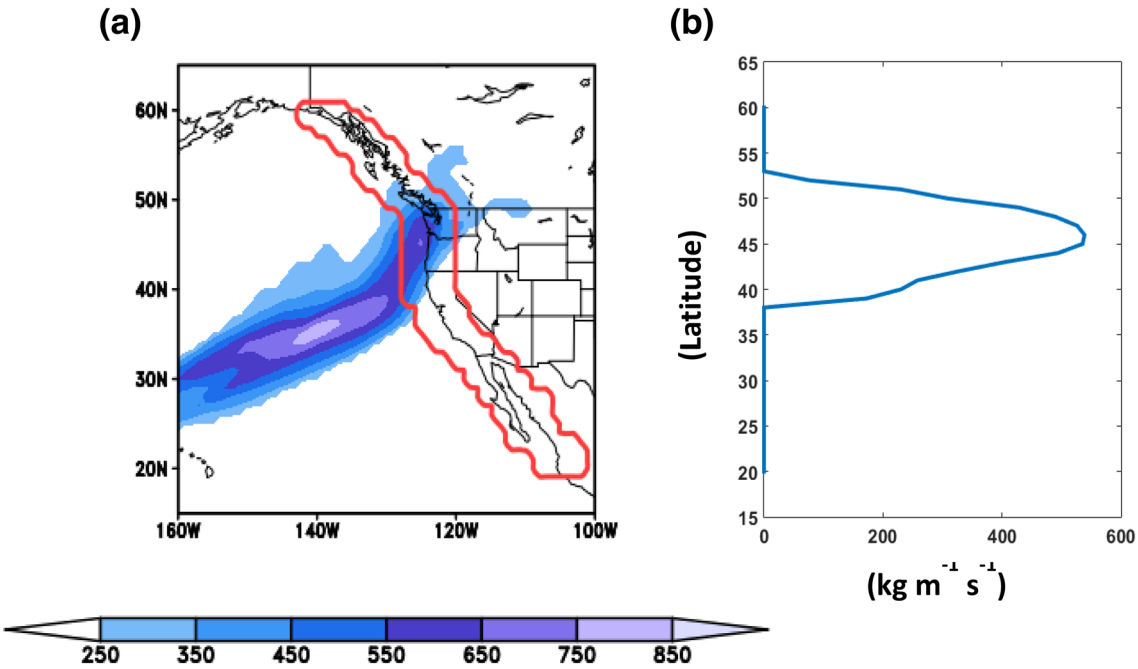

Fig. 3 **a** A landfalling AR event occurred on 28 January 2016. Shadings are the daily mean moisture flux (kg m^{-1} s^{-1}). **b** Zonally-averaged moisture flux along the coastal area (*red* contour in Fig. 3a). The latitude and the moisture flux values of the peak are selected as the landfall latitude and intensity. In this case, the landfall latitude is 46°N and landfall intensity 538.8 kg m^{-1} s^{-1}

Table 1 Characteristics of landfalling AR for climatology (CLIM, 37 years), EPEN (4 years), CPEN (4 years), and NINA (6 years)

	CLIM	EPEN	CPEN	NINA
Landfalling AR frequency (days/winter)	36.6	**40.5**	**39.8**	35.2
Mean landfall intensity (kg m^{-1} s^{-1})	393.8	384.9	408.1*	**377.8**
Mean landfall latitude (°)	43.1	43.4	**40.7***	43.2
Extreme landfalling AR frequency (days/winter)	9.2	8.0	12.3	**6.2**
(Southern Coast, 20°N–40°N) Landfalling AR frequency (days/winter)	17.7	19.5	**21.8**	16.3

Bold fonts indicate the values statistically significant from the CLIM at the 95% level estimated by the bootstrap resampling method

An asterisk (*) in CPEN category indicates that the value is significantly different (95% level) from the EPEN

CPEN and EPEN. The intensity and frequency of extreme landfalling ARs are the highest during CPEN.

Given that the effects of ENSO are realized through meridional shifts of the large-scale circulation patterns and associated AR moisture transport (Fig. 2), we compare the frequency distribution for landfalling ARs at different intensities and latitudes. Figures 4a and 5a show the distribution of climatological landfalling ARs frequency in each intensity (Fig. 4a, with a bin width of 50 kg m^{-1} s^{-1}) and latitude (Fig. 5a, with a bin width of 5°) category. The distribution of intensity ranges from 250 (which is the threshold for defining an AR) to 700 kg m^{-1} s^{-1}, with the maximum frequency occurring around 350 kg m^{-1} s^{-1} (Fig. 4a). The number of ARs greater than 700 kg m^{-1} s^{-1} is negligible. The distribution of the mean intensity for EPEN, CPEN, and NINA events is shown in Fig. 4b by the ratio of the intensity in each ENSO phase relative to climatology. In EPEN, the frequency of landfalling ARs in the moderate categories (300–400 kg m^{-1} s^{-1}) increases, while during CPEN, extreme landfalling ARs (>450 kg m^{-1} s^{-1}) generally occurs more frequently than the long-term mean. The number of extreme landfalling ARs in CPEN (12.3/year) is almost doubled compared to NINA winters (6.2/year) (Fig. 4b; Table 1).

The higher frequency of extreme landfalling ARs in CPEN is possibly due to a combination of the southward shift of the subtropical jet and Aleutian low (Fig. 1) and that the atmosphere is more humid at the lower latitudes which result in more moisture transport to North America. The mean latitude of landfalling ARs is shifted to the

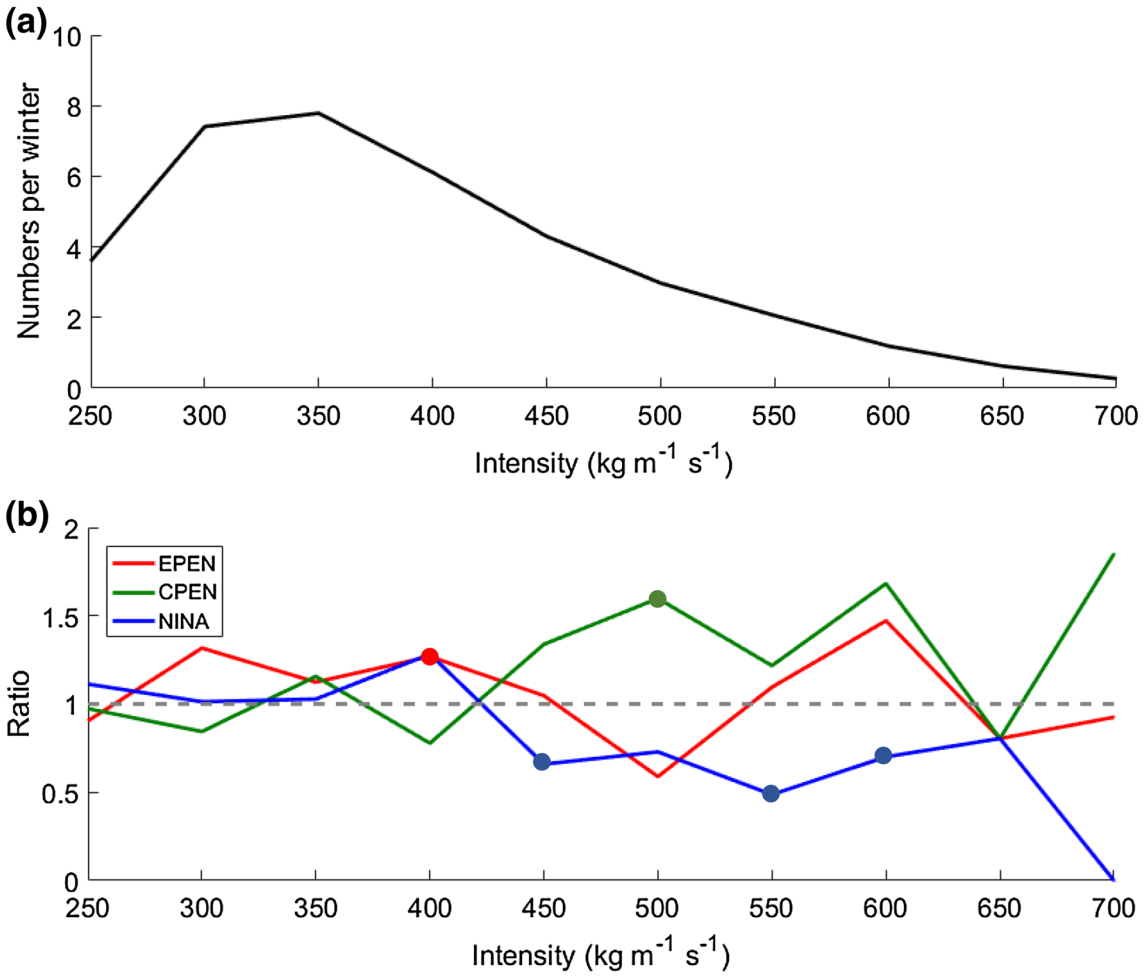

Fig. 4 **a** Distribution of climatological landfalling ARs frequency in each intensity category. **b** The ratio is the numbers in each ENSO phase to the climatology. The *gray dash line* indicates ratio equals to one. The *bold dots mark* the values that passed the 95% significance level based on a bootstrap method

south in CPEN (40.7°N) but stays almost the same in both EPEN (43.4°N) and NINA (43.2°N) relative to climatology (43.1°N) (Table 1). During EPEN, the mean latitude (43.4°N) does not match with the AR frequency map (Fig. 2) in which the frequency is anomalously high to the northwest US. The landfalling AR latitude does not necessarily match with the AR frequency map because only the peak values of AR intensity at a particular latitude is recorded as a landfalling AR, while all values that exceed the 250 kg m^{-1} s^{-1} criteria are taken into consideration for the AR frequency map (Fig. 2).

The occurrence of landfalling ARs ranges broadly from low to high latitudes with a peak near 45°N (Fig. 5a) and is not significantly different between EPEN and CPEN at higher latitudes (>35°N). At lower latitudes (20°N–35°N), the landfalling ARs frequency is considerably higher in CPEN and lower in EPEN relative to the climatology (Fig. 5). These results are consistent with the recent study by McCabe-Glynn et al. (2016) who showed that the extreme precipitation events affecting the southwest US, especially Southern California, are more likely during CPEN than EPEN.

4 Causes of change in seasonal moisture transport in response to ENSO

To investigate the mechanisms that cause the changes of moisture transport, and thus ARs, in the three ENSO phases, we analyzed the relative contributions of low-frequency and synoptic anomalies as well as the contribution from dynamic versus thermodynamic processes using the moisture budget equation. The moisture flux is split into components due to circulation and humidity anomalies, where either the wind (V) or specific humidity (q) can be

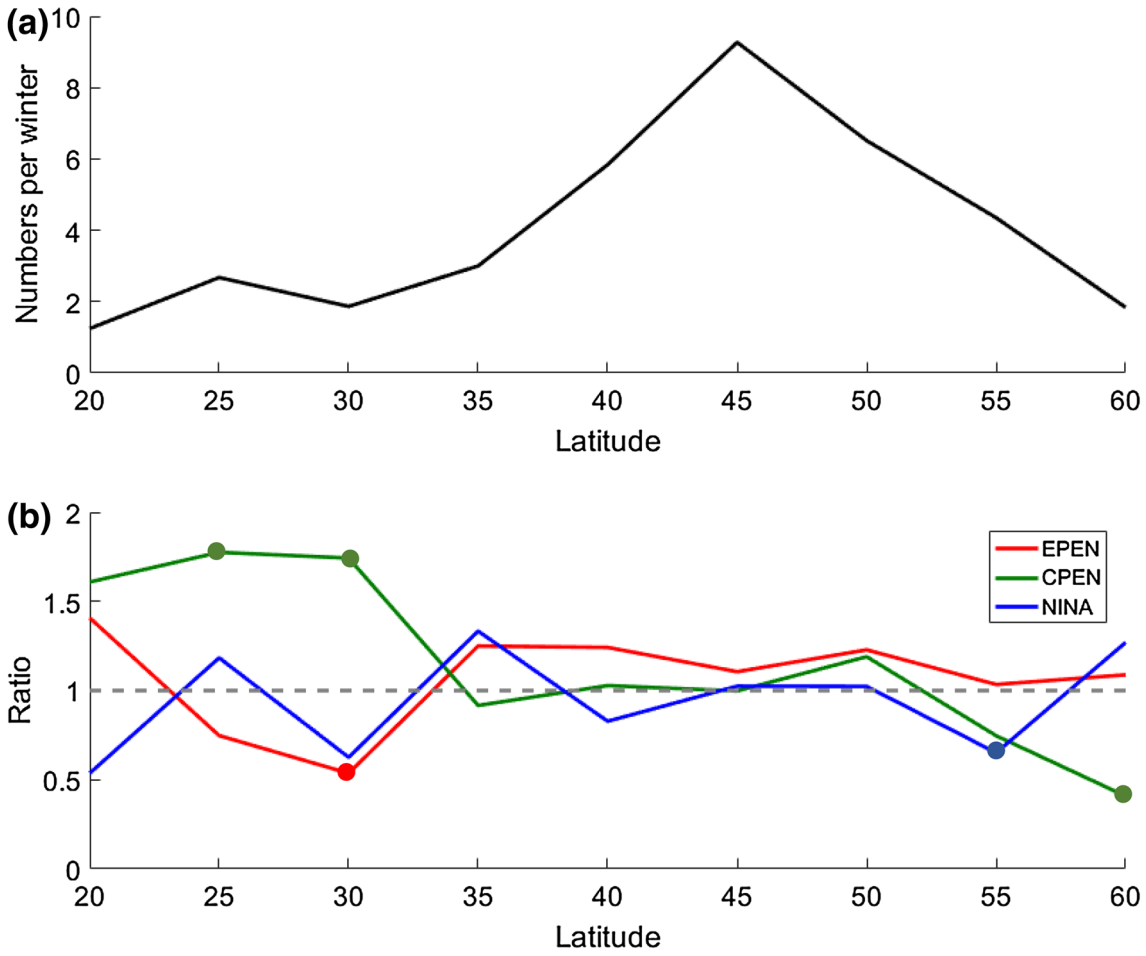

Fig. 5 Same as Fig. 4, except for landfalling AR latitude

held at climatological values while the other one is allowed to vary. Therefore, each term can be decomposed such as:

$$\begin{aligned} \bar{Q}^m &= \langle \bar{q}\bar{V} \rangle, \\ Q^{LF} &= \{ \langle \bar{q}V^{LF} + q^{LF}\bar{V} + q^{LF}V^{LF} \rangle \}, \\ Q^s &= \{ \langle \bar{q}V^s + q^s\bar{V} + q^sV^s \rangle \} \end{aligned} \tag{4}$$

where the angle bracket indicates the vertical integration from the surface to 300 hPa. The overbar is the climatology. The curly bracket indicates the seasonal (DJF) average of a particular year (e.g., EPEN). Composite analysis is performed on Q^{LF} and Q^s for the three ENSO phases. The climatology of the mean flow $\bar{Q}^m$ does not change among different ENSO phases. Note that the eddy cross terms (e.g., $V^{LF}q^s$) are negligible relative to the other terms (not shown).

4.1 Seasonal mean moisture transport

In the North Pacific, the mean climatological circulation primarily transports moisture zonally, while the low-frequency and synoptic anomalies transport moisture from ocean to land (Newman et al. 2012). Figure 6 shows the seasonal mean moisture flux (Q, vectors) and moisture flux divergence ($\nabla \cdot Q$, shading) for the climatology and for the anomalies for the three ENSO phases. The climatological moisture transport (Fig. 6d) is from the subtropics to the extratropics in the northeast Pacific, which roughly matches the area of AR frequency (Fig. 2d). The moisture flux convergence (blue shading) is the strongest in the coastal area while a complex divergence/convergence pattern occurs over the western US likely due to topography (Fig. 6d). During winter, evaporation and the moisture tendency are generally smaller than the other budget terms (Eq. 2) over the western North America, so the areas of moisture flux convergence and mean precipitation generally match each other (Fig. 7d). In EPEN winters, anomalous mean cyclonic flow in the northeast Pacific supports moisture transport to North America from central California to Alaska and induces strong moisture flux convergence and precipitation (Figs. 6a, 7a). In CPEN, due to the southward shift of the Aleutian Low, moisture is transported zonally

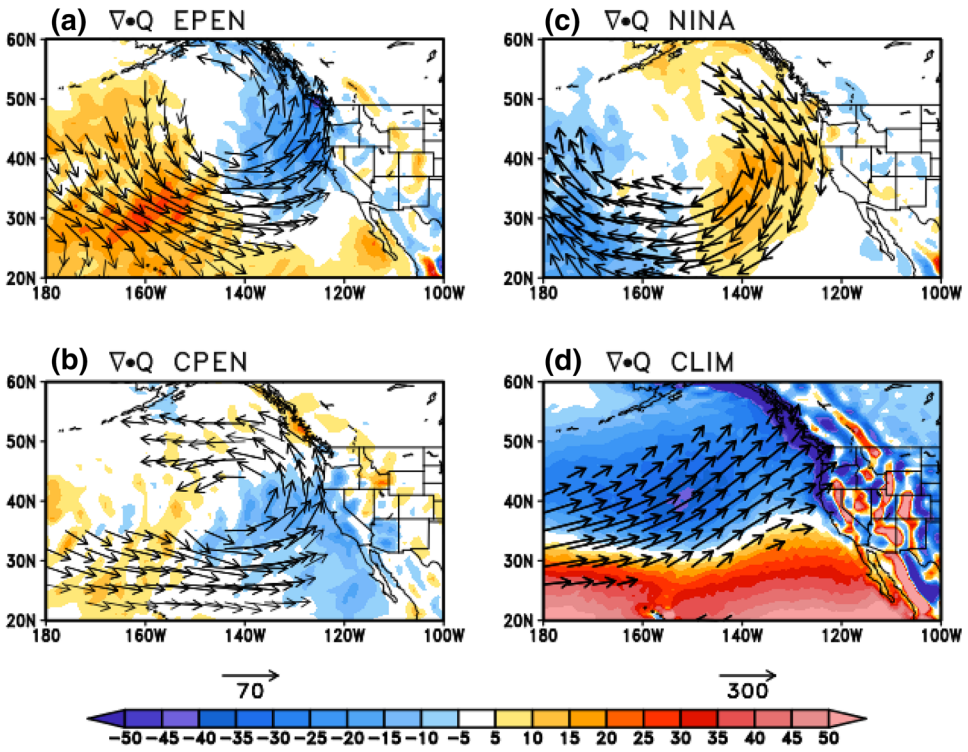

Fig. 6 Same as Fig. 2, except for the vertically integrated seasonal moisture flux divergence (*shading*, 10^{-6} kg m^{-2} s^{-1}). The vectors have exceeded the 95% significant level based on a bootstrap method

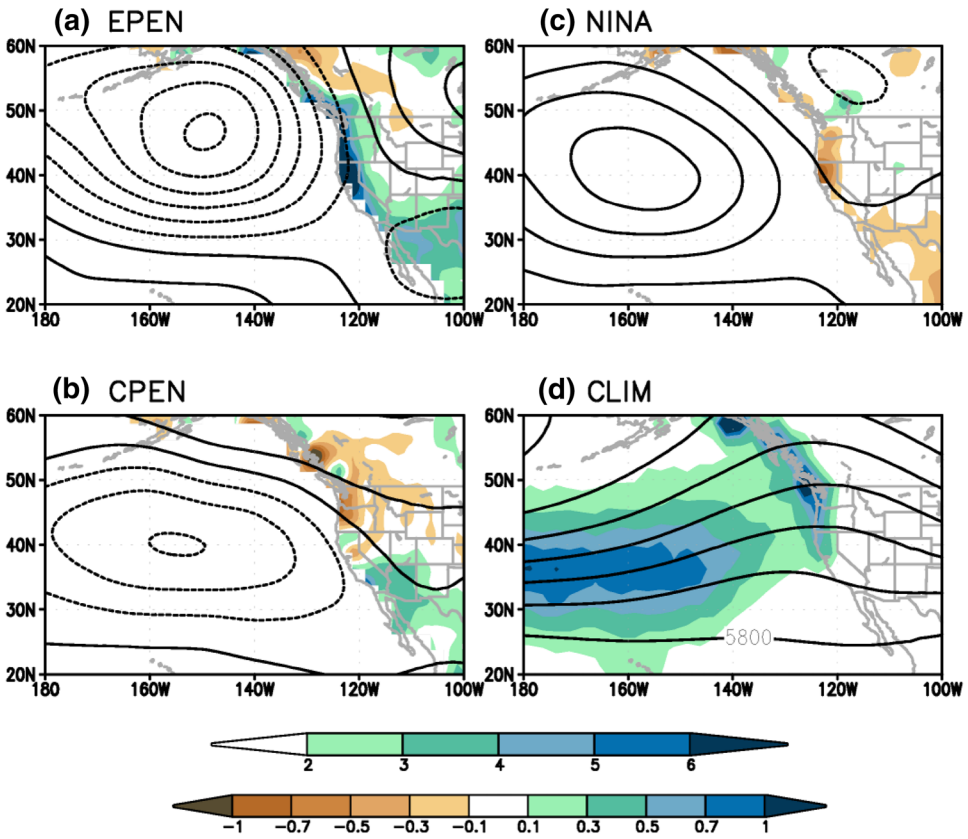

Fig. 7 Same as Fig. 2, except for precipitation (mm/day) and 500 hPa geopotential height (100 m interval for climatology and 20 m interval for anomalies)

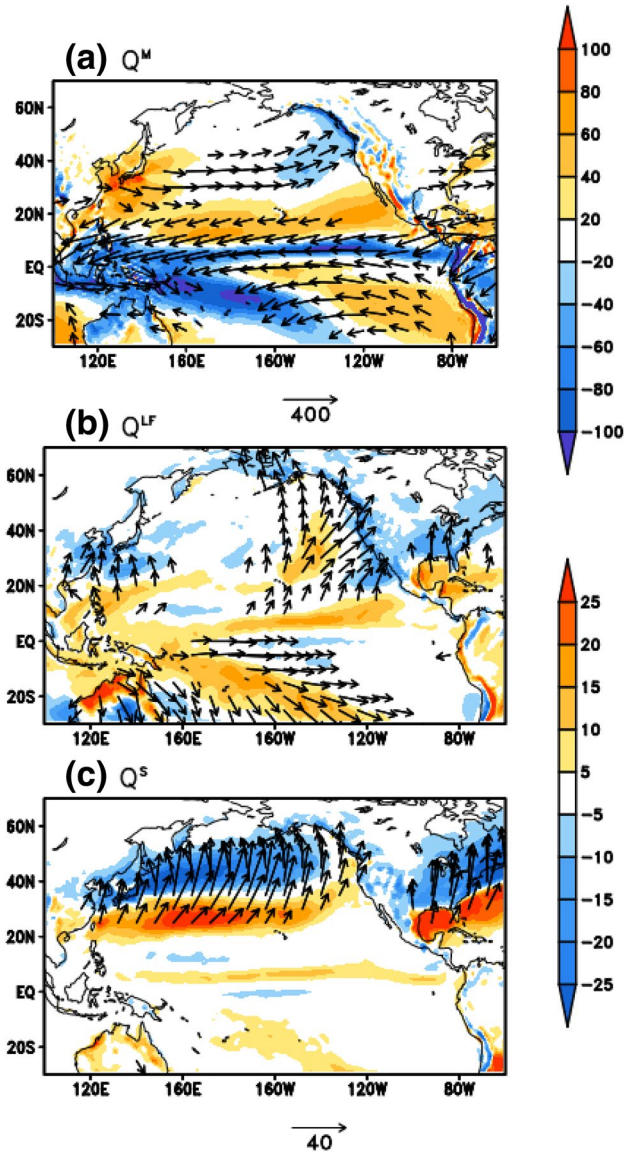

Fig. 8 Vertically integrated moisture flux divergence (*shading*, 10^{-6} kg m^{-2} s^{-1}) and moisture flux (vectors, kg m^{-1} s^{-1}) for long-term averaged **a** seasonal mean ($\bar{Q}^m$), **b** low frequency term ($\bar{Q}^{LF}$), and **c** synoptic term ($\bar{Q}^s$). Only values exceeding 100 kg m^{-1} s^{-1} in (**a**) and 10 kg m^{-1} s^{-1} in (**b**) and (**c**) are shown

between 20°–40°N, and stronger moisture convergence and precipitation is observed in the southwest US, particularly over the southwest US and Baja California (Figs. 6b, 7b). In NINA, anomalous divergence dominates near the west coast due to the anomalous anticyclonic flow over the eastern Pacific (Figs. 6c, 7c).

4.2 Low-frequency versus synoptic anomalies

The total moisture flux can be decomposed into the seasonal mean, low-frequency and synoptic anomalies, and residual terms (Eq. 3). Figure 8 shows the 37-year DJF mean moisture flux and moisture flux divergence $(\bar{Q}^m)$, low-frequency anomaly $(\bar{Q}^{LF})$ and synoptic anomaly $(\bar{Q}^s)$ derived from Eq. (4). This figure reproduces one previously found in Newman et al. (2012) using a different dataset and time period. When long-term averages are taken, the products of mean and anomalies (e.g., $\underline{\bar{q}V^{LF}}$) can be neglected and only transient term (e.g., $q^{LF}V^{LF}$) remain as shown in Newman et al. (2012). Generally, the moisture flux by the mean flow $(\bar{Q}^m)$ dominates the total moisture flux (Fig. 8a). Due to the dominant zonal wind in the Pacific, this term is mostly zonal with moisture flux divergence (moisture source) in the subtropics and convergence (moisture sink) in both the intertropical convergence zone (ITCZ) and South Pacific convergence zone (SPCZ). Over the northeastern Pacific, convergence occurs north of 30°N associated with poleward and eastward transport (Fig. 8a).

A primary moisture source for the contribution of the low-frequency anomalies $(\bar{Q}^{LF})$ to the long term mean is located to the northeast of Hawaiian Islands (Fig. 8b) and the low-frequency circulation transports the moisture to North America with strong convergence along the entire west coast (Fig. 8b). The change of the circulation by strengthening and weakening of the Aleutian Low and its corresponding moisture anomalies contribute to the low-frequency moisture transport (Newman et al. 2012). Newman et al. (2012) showed that the anomalous moisture gradient and the wind anomalies result in the same moisture transport pattern for both cyclonic and anticyclonic circulation anomalies that contribute to the mean pattern shown in Fig. 8b. In addition to low-frequency variability, Fig. 8c shows the contribution of long-term mean synoptic anomalies $(\bar{Q}^s)$ to the mean moisture flux. The moisture flux is nearly meridional with strong moisture flux convergence in the storm track across the North Pacific as was also found by Newman et al. (2012).

There is no distinction of $\bar{Q}^m$ between the ENSO phases, since $\bar{Q}^m$ is the long-term mean. To quantitatively determine the ENSO-related low-frequency and synoptic anomalies influences on the changes in seasonal mean moisture, low-frequency (Q^{LF}) and synoptic (Q^s) anomalies are composited for EPEN, CPEN and NINA (Fig. 9). The composites of moisture flux and moisture flux divergence for the low-frequency (Q^{LF}) anomalies in each ENSO phase (Fig. 9a–c) are similar to the seasonal mean anomaly (Fig. 6). Synoptic signals generally get averaged out over a season and result in weaker signal compared to the low-frequency variability (Fig. 9d–f). There are areas that are of similar magnitude to those in the low-frequency terms (Fig. 9a–c), but are noisier and not as large scale (Fig. 9d–f). Results from Fig. 9 indicates that seasonal mean moisture flux and its divergence are mostly due to the low-frequency anomalies with only secondary contributions from the synoptic anomalies.

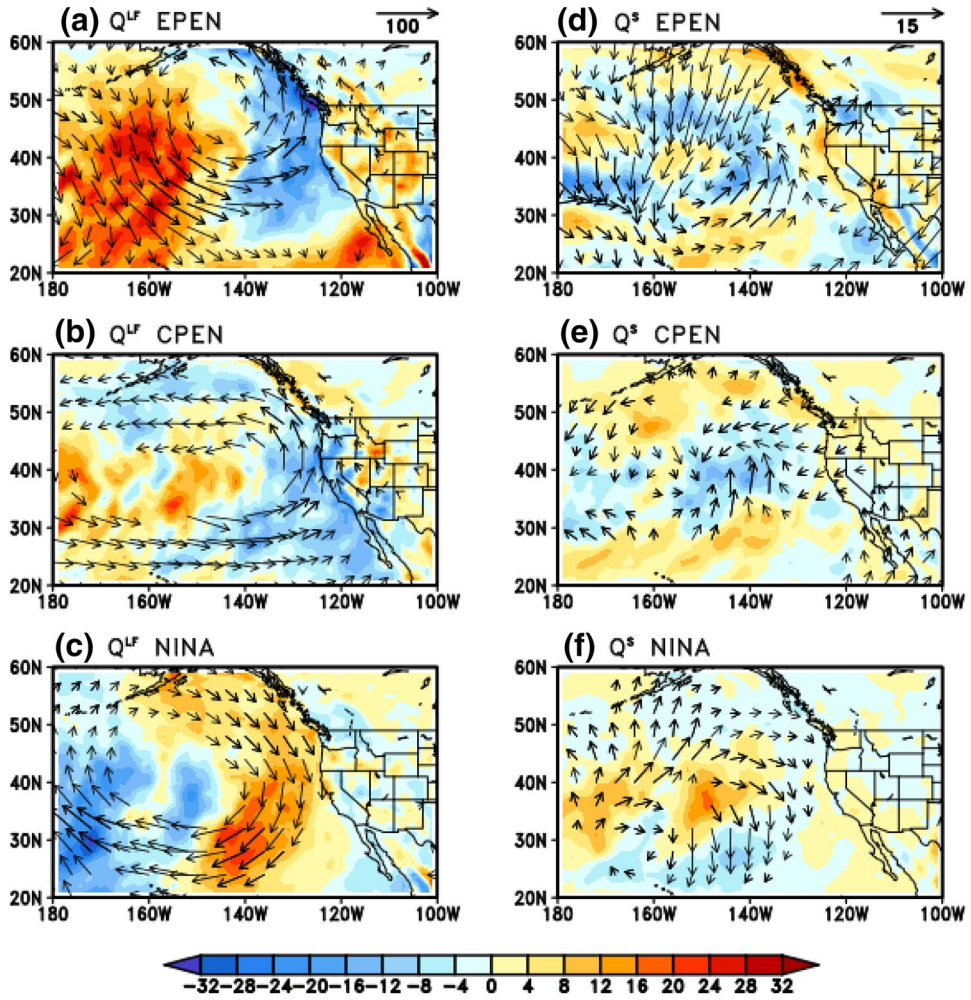

Fig. 9 Moisture flux divergence (*shading*, 10^{-6} kg m^{-2} s^{-1}) and moisture flux (vector, kg m^{-1} s^{-1}) for **a–c** low-frequency and **d–f** synoptic anomalies in (*top*) EPEN, (*middle*) CPEN, and (*bottom*) NINA. Vectors have passed the 95% significant level of *t* test

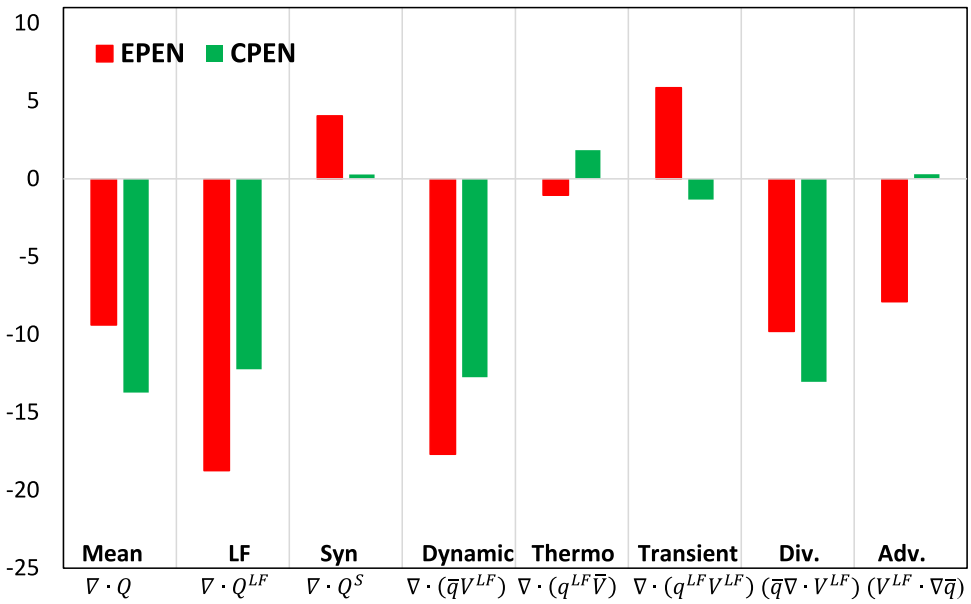

Fig. 10 Anomalies of moisture flux divergence for seasonal mean ($\nabla \cdot Q$), low-frequency (LF, $\nabla \cdot Q^{LF}$) and synoptic (Syn, $\nabla \cdot Q^{S}$) terms, low-frequency dynamic $\left(\nabla \cdot \left(\bar{q} V^{LF}\right)\right)$, thermodynamic $\left(\nabla \cdot \left(q^{LF} \bar{V}\right)\right)$, transient $\left(\nabla \cdot \left(q^{LF} V^{LF}\right)\right)$, mass-divergence $\left(\bar{q} \nabla \cdot V^{LF}\right)$, and advection $\left(V^{LF} \cdot \nabla \bar{q}\right)$ terms for EPEN (*red*, 45°N–60°N) and CPEN (*green*, 30°N–45°N). Units are 10^{-6} kg m^{-2} s^{-1}

To quantitatively compare the relative contribution of low-frequency and synoptic anomalies to the seasonal mean, each term is averaged over the west coast region where the seasonal moisture flux convergence (Fig. 6) has the largest impact. For simplicity, we compare the moisture flux divergence only for EPEN and CPEN. Selected areas are along the west coast (same as the region shown in Fig. 3) from 45ºN to 60ºN for EPEN and 30ºN to 45ºN for CPEN (Fig. 10). The low-frequency anomaly $\left(\nabla \cdot Q^{LF}\right)$ mainly contributes to the seasonal mean moisture flux divergence $(\nabla \cdot Q)$, while the contribution from the synoptic anomaly $(\nabla \cdot Q^{s})$ is relatively small (Figs. 9, 10). We will focus on the low-frequency anomalies from here on.

4.3 Dynamic versus thermodynamic processes

To further understand the processes that cause the low-frequency change of moisture flux divergence $\left(\nabla \cdot Q^{LF}\right)$ during the three ENSO phases, we separate the moisture flux divergence into its components. The low-frequency term of moisture flux contains three parts (Eq. 4): the mean moisture transported by the low-frequency wind anomaly (dynamic process, $\bar{q}V^{LF}$), low-frequency moisture anomaly transported by the mean wind (thermodynamic process, $q^{LF}\bar{V}$), and low-frequency moisture anomaly transported by low-frequency wind anomaly (transient, $q^{LF}V^{LF}$). Therefore, the low-frequency moisture flux divergence during each winter can be decomposed into:

$$\nabla \cdot Q^{LF} = \nabla \cdot \left(\bar{q}V^{LF}\right) + \nabla \cdot \left(q^{LF}\bar{V}\right) + \nabla \cdot \left(q^{LF}V^{LF}\right), \quad (5)$$

Figure 11a–c shows the first term on the right-hand side of Eq. 5, the dynamic process term $\left(\nabla \cdot \left(\bar{q}V^{LF}\right)\right)$. The patterns of this term (Fig. 11a–c), are similar to the low-frequency moisture flux divergence term (Fig. 9a–c), particularly for EPEN. The thermodynamic process term $\left(\nabla \cdot \left(q^{LF}\bar{V}\right)\right)$ and the transient term $\left(\nabla \cdot \left(q^{LF}V^{LF}\right)\right)$ are relatively small compared to the dynamic process term (not shown). The values of the three terms are averaged along the west coast and compared for EPEN and CPEN (Fig. 10). The dynamic process term $\left(\nabla \cdot \left(\bar{q}V^{LF}\right)\right)$ mainly contributes to the low-frequency moisture flux divergence, while the contribution of the thermodynamic and transient terms are relatively small (Fig. 10). Seasonal moisture transport in different ENSO years is dominated by dynamics to first order explained by changes in low-frequency circulation while changes in low-frequency moisture are less important.

4.4 Mass divergence versus advection

Given the small contribution of the thermodynamic and transient terms to the low-frequency moisture flux divergence (Fig. 10), we neglect these two terms and further decompose the dynamic process term in Eq. (5) as:

$$\nabla \cdot \left(\bar{q}V^{LF}\right) = \bar{q}\nabla \cdot V^{LF} + V^{LF} \cdot \nabla \bar{q}, \quad (6)$$

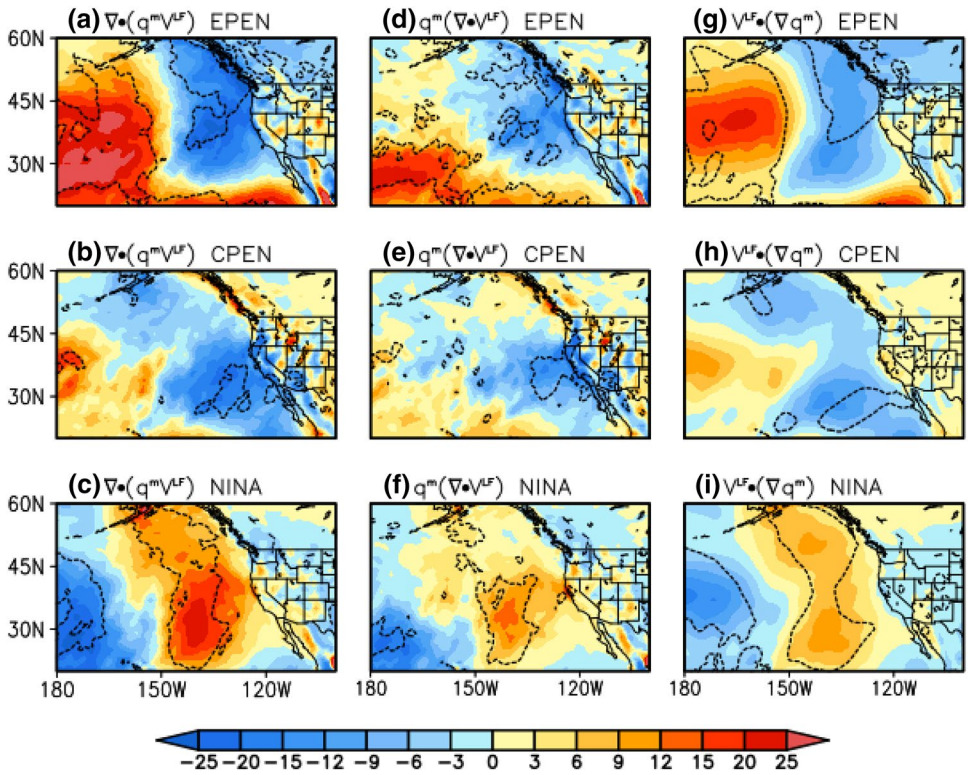

Fig. 11 Same as Fig. 9, except for (*left*) low-frequency dynamic $\left(\nabla \cdot \left(\bar{q}V^{LF}\right)\right)$, (*middle*) mass-divergence $\left(\bar{q}\nabla \cdot V^{LF}\right)$, and (*right*) advection $\left(V^{LF} \cdot \nabla \bar{q}\right)$ terms. *Dash* contours mark the regions that exceed the 95% significant *t* test level

where the first term on the right-hand side is the mass divergence by the low-frequency wind anomaly weighted by mean moisture (divergence term, $\bar{q}\nabla \cdot V^{LF}$) and the second term is the advection of mean moisture by low-frequency wind anomaly (advection term, $V^{LF} \cdot \nabla\bar{q}$). During the three ENSO phases, both the mass divergence and advection terms contribute to the dynamic process term with comparable magnitudes over the northeast Pacific (Fig. 11d–i). However, along the west coast, the contribution differs between EPEN and CPEN. During EPEN, the contributions of the divergence and advection terms along the northwest coast are comparable (Fig. 10), indicating that the moisture convergence by the low-frequency anomalous wind along the coast results from both the mass convergence and advection of moisture. However, during CPEN, along the southwest coast, the advection has reduced amplitude compared to the mass convergence (Fig. 11e, h), and the low-frequency moisture flux convergence results mainly from the mass convergence by the low-frequency wind, while the contribution from the advection is negligible (Fig. 10).

From these results, we conclude that the changes in moisture transport, to the west coast of North America in the three ENSO phases, are primarily due to the change of low-frequency wind. While both mass divergence and advection of moisture by the low-frequency wind are important during EPEN, the mass divergence plays a relatively important role in the moisture flux convergence along the southwest coast during CPEN.

5 Summary and discussion

The characteristics of atmospheric rivers and moisture transport in the northeast Pacific and western North America are investigated for ENSO events during winter (DJF) from 1979/80 to 2015/16 using daily aggregated and 6-hourly data from ERA-Interim. We compare the differences in AR characteristics (frequency, intensity, and landfall) and moisture transport between three ENSO phases: central Pacific El Niño (CPEN), eastern Pacific El Niño (EPEN), and La Niña (NINA). During EPEN, the subtropical jet extends to the south and the east with an anomalous cyclonic flow around a deeper Aleutian Low. More moisture is transported to the west coast of North America increasing the frequency of landfalling ARs. In CPEN, the Aleutian low shifts further south than in EPEN, increasing the number of ARs over the southwest US, including those of extreme intensity. In NINA, frequency of ARs reaching the US is reduced in association with the anomalous anticyclonic circulation over the northeast Pacific. Using the moisture budget equation, we diagnose the contribution of multiple factors to the seasonal mean moisture transport and conclude that the change in the low-frequency dynamic process by variations in the circulation as opposed to the changes in moisture is the main reason for the anomalous moisture transport in the three ENSO phases. The synoptic anomalies and low-frequency thermodynamic process do not contribute significantly to the seasonal mean moisture transport.

In the past several years, California experienced as severe a drought as has occurred for more than a century. The average precipitation for three recent consecutive 3 years, 2011/12 to 2013/14, was the second driest three-winter period since 1895 (Seager et al. 2014). As of November 2016, about 60% of California remains in severe drought according to the US Drought Monitor (http://droughtmonitor.unl.edu). 2011/12 was a La Niña year and El Niño conditions did not occur over the following 2 years (Seager et al. 2014). The frequency of landfalling ARs in California during 2011/12-2013/14 was far below normal. Based on our landfalling AR detection method, the long-term mean of the landfall frequency in California is 15.2/year, while the average during 2011/12-2013/14 winters was only 11.3/year. The last winter, 2015/16, was categorized as a strong EP El Niño event. The number of landfalling ARs along the west coast of North America (box in Fig. 3a) totaled 23 events but most of the ARs occurred over the northwest rather than the southwest.

Since ARs provide up to 30–50% of California's water supply (Dettinger et al. 2011), accurate prediction of ARs on sub-seasonal to seasonal timescales (S2S) is urgent. Accurate predictions of the occurrence, intensity and landfall position of ARs are difficult in numerical weather forecast models (Wick et al. 2013). While prediction skill of ARs beyond a week has not been assessed, several recent studies and our current study suggest an existence of potential predictability of ARs at S2S timescales (e.g., Guan and Waliser 2015; Kim and Alexander 2015). It is often easier to predict so-called "sources of predictability" such as ENSO or MJO than to predict their downstream effects such as the location, frequency, and intensity of ARs. The MJO is the dominant tropical sub-seasonal phenomenon that modulates ARs in the northeast Pacific (Guan et al. 2012; Guan and Waliser 2015). Therefore, the link between low-frequency climate variability, including the MJO, and ARs presents a potential source of S2S prediction of Atmospheric Rivers and the associated extreme winter precipitation in the western US.

Acknowledgements Constructive and valuable comments from Dr. Matthew Newman (NOAA/ESRL) and two anonymous reviewers are greatly appreciated. The authors would like to thank Mr. Lequan Chi for helping with the AR detection coding. This study was supported by NOAA's CPO MAPP under Grant NA15OAR4310078 and the KMA R&D Program under Grant KMIPA 2016–6010.

References

Alexander MA, Scott JD, Swales D, Hughes M, Mahoney K, Smith CA (2015) Moisture pathways into the US intermountain west associated with heavy winter precipitation events. J Hydrometeorol 16:1184–1206

Bao J-W, Michelson SA, Neiman PJ, Ralph FM, Wilczak JM (2006) Interpretation of enhanced integrated water vapor bands associated with extratropical cyclones: their formation and connection to tropical moisture. Mon Weather Rev 134:1063–1080

Capotondi A, et al (2015) Understanding ENSO Diversity. Bull Am Meteorol Soc 96:921–938

Chang EKM, Zheng C, Lanigan P, Yau AMW, Neelin JD (2015) Significant modulation of variability and projected change in California winter precipitation by extratropical cyclone activity. Geophys Res Lett 42:5983–5991

Dee DP et al (2011) The ERA-Interim reanalysis: configuration and performance of the data assimilation system. Q J R Meteorolog Soc 137:553–597

Dettinger MD (2006) Fifty-two years of pineapple-express storms across the West Coast of North America. Report CEC-500-2005-004.

Dettinger MD, Ralph FM, Das T, Neiman PJ, Cayan DR (2011) Atmospheric rivers, floods and the water resources of California. Water 3:445–478

Gimeno L, Nieto R, Vázquez M, Lavers D (2014) Atmospheric rivers: a mini-review. Front Earth Sci 2(2). doi:10.3389/feart.2014.00002

Guan B, Waliser DE (2015) Detection of atmospheric rivers: Evaluation and application of an algorithm for global studies. J Geophys Res Atmos 120:12514–12535

Guan B, Waliser DE, Molotch NP, Fetzer EJ, Neiman PJ (2012) Does the Madden-Julian oscillation influence wintertime atmospheric rivers and snowpack in the Sierra Nevada? Mon Weather Rev 140:325–342

Guan B, Molotch NP, Waliser DE, Fetzer EJ, Neiman PJ (2013) The 2010/2011 snow season in California's Sierra Nevada: Role of atmospheric rivers and modes of large-scale variability. Water Resources Res 49:6731–6743

Kim H-M, Alexander MA (2015) ENSO's modulation of water vapor transport over the Pacific–North American region. J Clim 28:3846–3856

Kim H-M, Webster, Peter J, Curry JA (2009) Impact of shifting patterns of Pacific Ocean warming on North Atlantic tropical cyclones. Science 325:77–80

McCabe-Glynn S, Johnson KR, Strong C, Zou Y, Yu J-Y, Sellars S, Welker JM (2016) Isotopic signature of extreme precipitation events in the western US and associated phases of Arctic and tropical climate modes. J Geophys Res Atmos 121:8913–8924

Mundhenk BD, Barnes EA, Maloney ED (2016) All-season climatology and variability of atmospheric river frequencies over the North Pacific. J Clim 29:4885–4903

Neiman PJ, Ralph FM, Wick GA, Lundquist JD, Dettinger MD (2008) Meteorological characteristics and overland precipitation impacts of atmospheric rivers affecting the West Coast of North America based on eight years of SSM/I satellite observations. J Hydrometeorol 9:22–47

Neiman PJ, Schick LJ, Ralph FM, Hughes M, Wick GA (2011) Flooding in Western Washington: the connection to atmospheric rivers. J Hydrometeorol 12:1337–1358

Newell RE, Newell NE, Zhu Y, Scott C (1992) Tropospheric rivers?—a pilot study. Geophys Res Lett 19:2401–2404

Newman M, Kiladis GN, Weickmann KM, Ralph FM, Sardeshmukh PD (2012) Relative contributions of synoptic and low-frequency eddies to time-mean atmospheric moisture transport, including the role of atmospheric rivers. J Clim 25:7341–7361

Payne AE, Magnusdottir G (2014) Dynamics of landfalling atmospheric rivers over the North Pacific in 30 years of MERRA reanalysis. J Clim 27:7133–7150

Peixoto JP, Oort AH (1992) Physics of climate. American Institute of Physics, New York

Ralph FM, Neiman PJ, Wick GA, Gutman SI, Dettinger MD, Cayan DR, White AB (2006) Flooding on California's Russian river: role of atmospheric rivers. Geophys Res Lett 33:L13801

Rayner NA et al (2003) Global analyses of sea surface temperature, sea ice, and night marine air temperature since the late nineteenth century. J Geophys Res Atmos 108:4407

Rutz JJ, Steenburgh WJ, Ralph FM (2014) Climatological characteristics of atmospheric rivers and their inland penetration over the western United States. Mon Weather Rev 142:905–921

Rutz JJ, Steenburgh WJ, Ralph FM (2015) The Inland penetration of atmospheric rivers over Western North America: a lagrangian analysis. Mon Weather Rev 143:1924–1944

Ryoo J-M, Kaspi Y, Waugh DW, Kiladis GN, Waliser DE, Fetzer EJ, Kim J (2013) Impact of Rossby wave breaking on US west coast winter precipitation during ENSO events. J Clim 26:6360–6382

Seager R, Naik N, Vogel L (2012) Does global warming cause intensified interannual hydroclimate variability? J Clim 25:3355–3372

Seager R, Hoerling M, Schubert S, Wang H, Lyon B, Kumar A, Nakamura J, Henderson N (2014) Causes and predictability of the 2011–14 California drought, DTF/NIDIS Assessment Report, doi:10.7289/V58K771F

Smith CA, Sardeshmukh P (2000) The effect of ENSO on the intraseasonal variance of surface temperature in winter. Int J Climatol 20:1543–1557

Smith BL, Yuter SE, Neiman PJ, Kingsmill D (2010) Water vapor fluxes and orographic precipitation over northern California associated with a landfalling atmospheric river. Mon Weather Rev 138:74–100

Trenberth KE (1991) Climate diagnostics from global analyses: conservation of mass in ECMWF analyses. J Clim 4:707–722

Wick GA, Neiman PJ, Ralph FM, Hamill TM (2013) Evaluation of forecasts of the water vapor signature of atmospheric rivers in operational numerical weather prediction models. Weather Forecast 28:1337–1352

Xie P, Arkin PA (1997) Global precipitation: a 17-year monthly analysis based on gauge observations, satellite estimates, and numerical model outputs. Bull Am Meteorol Soc 78:2539–2558

Yu J-Y, Zou Y (2013) The enhanced drying effect of Central-Pacific El Niño on US winter. Environ Res Lett. doi:10.1088/1748-9326/8/1/014019

Zhu Y, Newell RE (1998) A proposed algorithm for moisture fluxes from atmospheric rivers. Mon Weather Rev 126:725–735